Strike-slip fault segmentation: Insight from numerical modeling

Work Package #1 "Fault and Tectonics"

AUTHORS		REVIEW		APPROVAL	
Name	Date	Name	Date	Name	Date
Yann Klinger *Liqing Jiao*	*2021/07/22*	*Thierry Camelbeeck* *Ian Main* Ian Main	*2021/*.08/.17	*Emmanuel VIALLET* ***Public-access..........*** ☒ ***SIGMA-2 restricted...*** ☐	*2021/...../.....*

Document history

DATE	VERSION	COMMENTS
2021/07/22	*2*	*This is the revised version of the report. The next text includes at best comments from the two internal reviews*

Executive summary

Understanding fault geometry and how it might impact surface deformation.

From models to field observation

Y. Klinger, L. Jiao, L. Scholtès

July 22nd 2021

This text is intended to remind the framework of this project, the final scientific objectives, and the current state of the project, including this deliverable.

Framework and scientific objectives of this project:

In continental setting it is often possible to recognize active tectonic structures based on specific geomorphology, even in context of slow intra-plate deformation. In many cases, even in places with low rate of deformation, a careful examination of active fault traces allows identifying some level of geometrical complexity with linear fault segments bounded by relay zones. This is especially true for strike-slip faults, which are common structures in intra-plate tectonic domain. However, how much surficial geometrical complexities are reflective of the fault geometry at depth and how much such complexity could influence earthquake processes are still highly debated. Field observations of large-magnitude earthquakes surface ruptures, as well as analogue experiments, suggest that this complexity is real and exists at depth as well. However, by nature, these observations are limited to provide further insights into the understanding of processes related to fault growth, fault structure, and earthquake deformation. Indeed, we cannot access the physical parameters controlling the different processes pertaining to the deformation and, most of the time, our observation is limited to snapshots in time without a vision of the long-term evolution of the structures.

The current proposal aims at better understand the structural properties of faults, the time evolution of the fault structure, and at its impact on earthquake processes and surface deformation.

In this project, we propose to develop a model of strike-slip fault using the discrete element modeling technic. The critical advantage of this technic for this class of problem is that there is no need to prescribe a fault geometry a-priori. This technic is based on the modeling of a large number of particles, which interactions are controlled by the boundary conditions and by inter-particles rules that can reproduce characteristics of different crustal rheologies. In this project we first grow a strike-slip fault network to study how the fault segmentation is sensitive to the different model parameters, and in particular to the thickness of the brittle layer. In a second part we will see how deformation is accommodated on and off the main fault zone and compare these results with field observations. Eventually, if these two phases are successful, we plan on simulating earthquake rupture in the numerical model.

State of realization of the project:

This project has been awarded funding for 2 years. The funding is covering the full salary of L. Jiao, postdoctoral fellow at IPGP. Any other expenses related to the project, including the acquisition of a powerful computer station to run simulation and participation to scientific meetings, are funded by IPGP. L. Jiao has been hired at IPGP on May 1st, 2019. Thus, this report covers about 2 years of work during which period L. Jiao had to settle in France (she came from Singapore where she completed her PhD), get acquainted with the project, and produce results. Overall she has been doing very well and she has been able to present a first set of results at AGU in December 2019. If things would have gone as planned she would have been joining Y. Klinger in UC Berkeley, USA, in February-March 2020 to finalize this part of the work and start the next step. Unfortunately, the unforeseen covid-19 crisis has stepped-in, which has changed the pace of the project. L. Jiao got first stuck in France, and eventually moved back to Singapore and then to China mid-March 2020, closer to her relatives, where she stayed until September 2020. No need to say that this event has seriously slowed down the realization of the project. Here, you will find attached the final version of this deliverable. It corresponds to the revised version of the manuscript that was submitted to *Geophysical Research Letter* on July 2nd 2021. In fact the comments provided by I Main and T. Camelbeeck in their internal review are very similar to some of the comments by the *GRL* reviewers. Hence, you will notice that most of the comments are addressed in this revised version. In particular, some of the questions about comparison between FDM and DEM are fully addressed in the supplementary material of the paper. One suggestion about presenting more of the influence of the different physical parameters on the results has, however, being left outside the current manuscript for sake of space. A second manuscript, more technical, is currently being written that would eventually present all our sensibility studies. Most of the presentation issues noted by the two reviewers have also been addressed in this new version of the deliverable. Thus we hope that you will find this updated deliverable satisfactory.

Main results presented in the current draft:

this final report presents solid and interesting results which are summarized down below:

- We have been able to set up an experiment with dimensions large enough that we can confidently exclude boundary effects when propagating a strike-slip fault.
- We have been able to test that the rheological parameters that we are using in our model reproduce well the mechanical behavior of the upper crust at the different depths considered, validating our set-up.
- We have been able to run strike-slip experiments with different model thickness, from 16 km to 3 km (we wanted to go to 20 km but unfortunately we currently do not have access to the computer for extra calculations, as it is switched off at IPGP) and to measure inter-Riedel distance, which is our proxy for fault segment. We can show the linear dependency of this distance with the thickness of the model, which confirms the primary control of the thickness of the brittle material on the inter-Redel distance. We have conducted additional tests to test the sensitivity of our results to variation of the other free parameters of the model. We show that they have only minor effect.
- We have been able to compare our numerical results with natural observation and analogue experiment results. They are all consistent and we show that the ratio of the thickness over distance remains in the same range for all kind of observations, pointing to similar physics processes.
- We have investigated the physical processes behind our observations, and more specifically the spatial distribution of the Riedel along strike, which controls the value of the ration between

thickness and inter-Riedel distance. Using a finite difference modeling approach and following previous results by Bai and Pollard (2000), we could show that for a specific thickness and set of rheological parameters, the state of stress in the model dictates the maximum distance between two successive Riedels, a process that has been coined the fracture saturation in the literature.

Fault Segmentation Pattern Controlled by Thickness of Brittle Crust

L. Jiao[1], Y. Klinger[1], and L. Scholtes[2]

[1] Université de Paris, Institut de physique du globe de Paris, CNRS, Paris, France.

[2] Université Clermont Auvergne, CNRS, IRD, OPGC, Laboratoire Magmas et Volcans, Clermont-Ferrand, France.

Corresponding author: Yann Klinger (klinger@ipgp.fr)

Revised version submitted to *Geophys. Res. Let.* On July 2nd 2021

Key Points:

- Shear fractures, including earthquake ruptures, are spatially segmented following a pattern inherited from early fracture development
- Numerical simulations show both upward and downward crack propagation when a brittle layer is subjected to strike slip faulting
- Fault segmentation is spatially organized to maintain the material in a stable compressive state of stress through localized tensile ruptures.

Abstract

During large earthquakes, seismic sources tend to split in several sub-events that rupture neighboring fault patches called fault segments. The scaling of such segmentation plays a decisive role in earthquake rupture dynamics, especially for strike-slip events. Using numerical modeling we demonstrate that when a pristine layer of brittle material is sheared, the first oblique Riedel fractures nucleate with a regular spacing that is controlled by the thickness of that layer. During later localization of the deformation, those initial fractures control the spatial structuration of the entire fault system. Analyzing the horizontal stress distribution in fault-parallel direction for different ratios between inter-Riedel distance and material thickness, we identify a threshold at 1.5, beyond which the stress switches from compressional to tensional and leads to the nucleation of a new Riedel fracture. Thus, the inter-Riedel segment length appears to be controlled by the vertical distribution of stress along the fault.

Plain Language Summary

Geologic faults, including strike-slip faults, are not continuous smooth structures. Detailed fault mapping and earthquake rupture traces show that they are rather formed by discontinuous segments bounded by jogs and bends. The structure of faults impacts the way a rupture propagates during an earthquake, and eventually where the earthquake rupture starts and stops. Although such spatial organization as long been noted from natural observations and analogue experiments, the physical processes presiding at such organization remain elusive. In this work, we use numerical experiments to show that the fracture pattern is primarily controlled by the thickness of the brittle part of the crust of the Earth and that there is a critical ratio between inter-fracture distance and thickness for which the system is stable and does not need to rupture to accommodate shear. The value, ~1.5, of this ratio is found to be the same in our numerical models, in analogue sand experiments, and for real earthquake ruptures, pointing to a universal physical process.

1 Introduction

When brittle materials are sheared beyond their elastic threshold, stress is released through fractures (Conner *et al.*, 2003; Taheri *et al.*, 2020). In the case of the crust of the Earth it may corresponds to earthquake ruptures that produce finite deformation. In the case of continental deformation, when the maximum compressional stress is horizontal, deformation tends to localize along strike-slip faults such as the San Andreas Fault. During medium to large earthquakes with magnitude M≥6.5, most earthquake ruptures involve the entire seismogenic brittle crust, which thickness is 15±5km in continents (Klinger, 2010; Scholz, 1990), and break the ground surface . Field studies (Wechsler *et al.*, 2010), space geodesy (Wei *et al.*, 2011), and seismology (Bilham and Williams, 1985) have long brought evidence that strike-slip earthquake ruptures produce spatially segmented fracture patterns on the ground surface (Fig. 1a), with segment length scaling with the thickness of the brittle crust (Klinger, 2010). These segments are usually bounded by relay zones or bends. Analogue experiments have also hinted at the correlation between the spatial distribution of fractures and the thickness of sheared brittle materials (Cambonie *et al.*, 2019; Lefevre *et al.*, 2020).

Here, we use numerical experiments to test further this correlation, explore the kinematics of fracture growth leading to this peculiar spatial pattern, and derive a universal physical process that explains the relationship between the brittle thickness and the segment length.

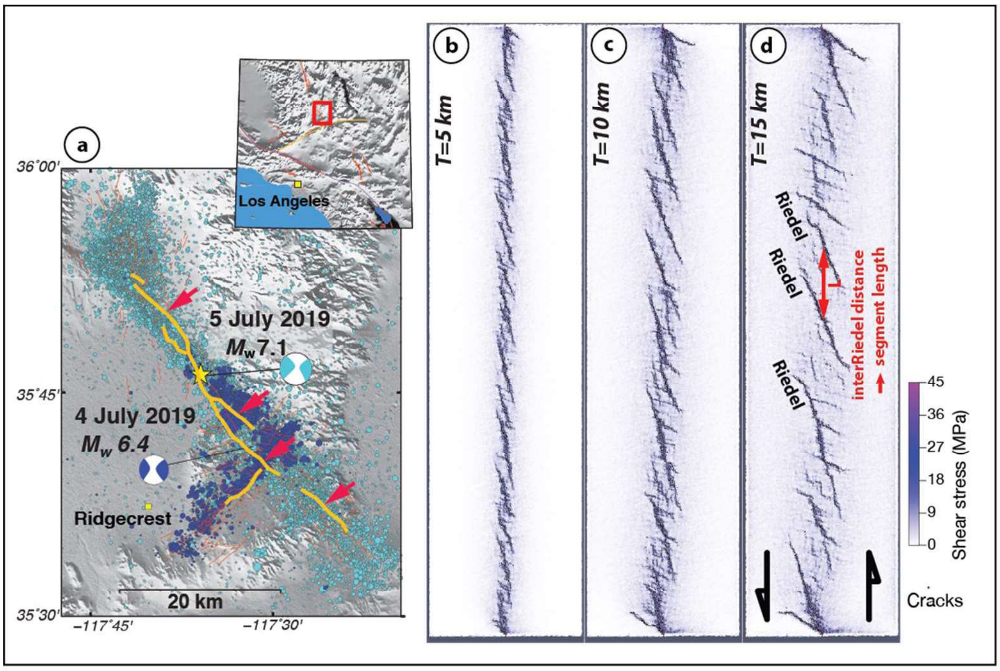

Figure 1: a) Surface rupture for the Ridgecrest Earthquake. Individual segments (Y-shear fractures) are indicated by red arrows (after Ross et al., 2019). b) to d) Top views of left-laterally sheared DEM models with different thicknesses T. Riedel shears nucleate to accommodate shear. The segment length L corresponds to the inter-Riedel distance L measured along the direction of shear. These segments correspond to Y-shear fractures.

2 Discrete element modeling of fault growth

Geological fault structures, including strike-slip fault systems, have long been studied through numerical modeling (Lynch and Richards, 2001; Segall and Pollard, 1980). However, classical modeling approaches, like the finite element method (FEM) or the finite difference method (FDM), implement faults as pre-existing discontinuities embedded within the numerical medium, therefore hindering mechanical investigation of any spatio-temporal evolution of fault geometry. Conversely, the discrete element method (DEM) enables to simulate the nucleation and propagation of discrete structures by representing the medium as a collection of independent particles interacting one with another through predefined force-displacement laws (Cundall and Strack, 1979; Potyondy and Cundall, 2004; Scholtès and Donzé, 2012). Commonly used to tackle geomechanics problems, the DEM has been successfully applied to study fault system formation or pull-apart basin, including strike-slip settings (Fournier and Morgan, 2012; Liu and Konietzky, 2018; Morgan, 1999; Morgan and Boettcher, 1999).

In this study, we model the continental brittle crust using a bonded particle model implemented in the YADE DEM open-source software (Scholtès and Donzé, 2013; Šmilauer *et al.*, 2015). The particles forming the medium interact through elastic brittle inter-particle laws, which are calibrated so that the emergent bulk behavior of the simulated medium corresponds to the pressure dependent behavior of a typical elastic cohesive brittle rock (see Supplementary Material for details of the methodology, the model formulation as well as for illustration of the emergent behavior). To study strike-slip faulting in the brittle crust, we built up three dimensional models of dimensions equal to *160 km* x *40 km* x *T,* with thicknesses T ranging from 3 km to 30 km (Fig. S2). The models are made up of spherical particles whose radii are uniformly distributed between 170 m and 320 m. The particle density was adjusted as function of the porosity of the particle packing so that the bulk density of the layer corresponds to the crust density (Table S1). Our synthetic crust thus consists of an initially intact and homogeneous elastic brittle layer with boundary conditions set up to mimic a strike-slip tectonic setting. The top surface of the layer is free, while roller type boundary conditions are defined on the three other sides (the normal displacements along the boundary walls are blocked). In the first stage of the loading sequence, internal stresses are generated by letting the layer stabilize under gravity. Due to the boundary conditions, the major principal stress at the end of this preconditioning stage is vertical and equal to the lithostatic stress, and the horizontal stresses result from the Poisson effect. Then, this pre-stressed layer is sheared horizontally by imposing opposite and parallel constant velocities on each of its half through the lateral and bottom boundaries (Fig. S2). No additional stresses were considered in this study other than the ones induced by the initial gravitational settling and subsequent shear loading. Also, the loading rate was chosen to ensure the model response remains quasi-static (rate independent) during the entire deformation process (Fig. S4).

During strike-slip deformation, the localization of deformation is twofold (Naylor *et al.*, 1986). In a first stage, a set of distinct Riedel-shears appears on the top free surface of the medium, which are oblique to the shear direction. During a second stage, Y-shear fractures develop in between successive Riedel-shears, parallel to the shear direction. These Y-shears would eventually coalesce to form a through-going shear fault if the deformation is continued. In our models, the inter-Riedel Y-shears are analogue for fault segments observed in natural strike-slip systems (Fig. 1) and are thus called segments hereafter. To study the influence of the crust thickness on this localization process, we varied the thickness T of our synthetic layer between 3km and 30km (keeping the same model resolution for all cases). For $T \leq 3$ km, no Riedel-shears would appear and a through-going shear fault formed from the beginning of the experiment. Fig. 1b to 1d show examples of surface fault patterns obtained for thicknesses T respectively equal to 5, 10, and 15 km, just before the appearance of the inter-Riedel Y-shears (see additional simulations for other thicknesses in Fig. S6). The associated horizontal offsets are respectively equal to 86 m, 156 m, and 174 m. The average distance between two successive Riedel-shears, distance hereafter called segment length, is determined by dividing the total number of Riedel-shears by the total length of the model (160 km). Our numerical results show that for T=5 km (Fig. 1b), the number of segments is 18, with an average length of 8.9 km per segment, for T=10 km (Fig. 1c), the model produces 11 segments, with an average length of 14.5 km, and for T=15 km (Fig. 1d), the model produces 10 segments, with an average length of 16 km (see Table S2 for Riedel-shears count, segment length, and uncertainties for all simulations). Therefore, our numerical simulations show that the segment length L increases linearly with the layer thickness T (Fig. 2).

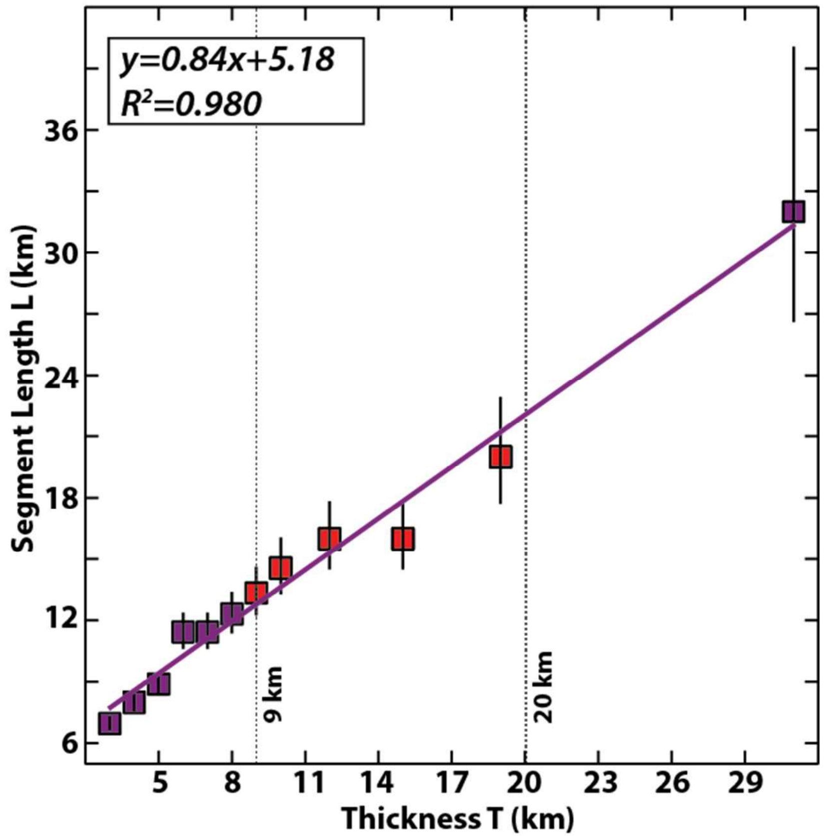

Figure 2: Linear relationship between segment length L and thickness T observed in sheared brittle layers simulated with the DEM. Red squares indicate the range of values commonly accepted for the brittle continental crust thickness (9km≤T≤20km).

3 Temporal evolution of fracture growth

Analogue experiments (Naylor *et al.*, 1986) and theoretical derivation (Mandl, 1999) have suggested that Riedel-shears would initiate at the basal discontinuity of the brittle layer and grow upward, following an helicoidal trajectory, which corresponds to the most effective geometry for energy dissipation (Francfort and Marigo, 1998).

Our numerical simulation reveals that soon after the proto-Riedel shear cracks start to propagate upward from the basal shear zone (step 50 in Fig. 3), some cracks also start to nucleate at the surface (step 65 in Fig. 3). Unlike the cracks that are uniformly distributed along the basal shear zone, the cracks initiating at the surface are spatially clustered (step 70 in Fig. 3). These cracks then propagate downward (step 80 in Fig. 3) to link with the upward crack front (step 100 in Fig. 3) and to form full-grown Riedel shears (see also animation A1).

Eventually, our model shows that the spatial distribution of the crack clusters at the surface of the layer controls the distance between successive Riedel-shears.

The nucleation and propagation of cracks within bonded particle models are driven by the distribution of stress within the simulated medium. Cracks develop in places where inter-particle bonds cannot bear the excess of stress due to either tensile or shear mechanisms. In order to get further insights into the mechanisms at play during the faulting preocess, we investigated the state of stress on an idealized plane located between two successive Riedel-shears (Fig. 4a) as a function of the ratio between thickness of the model and segment length using a purely elastic 2D model (see Supplementary Material for additional information about model setting).

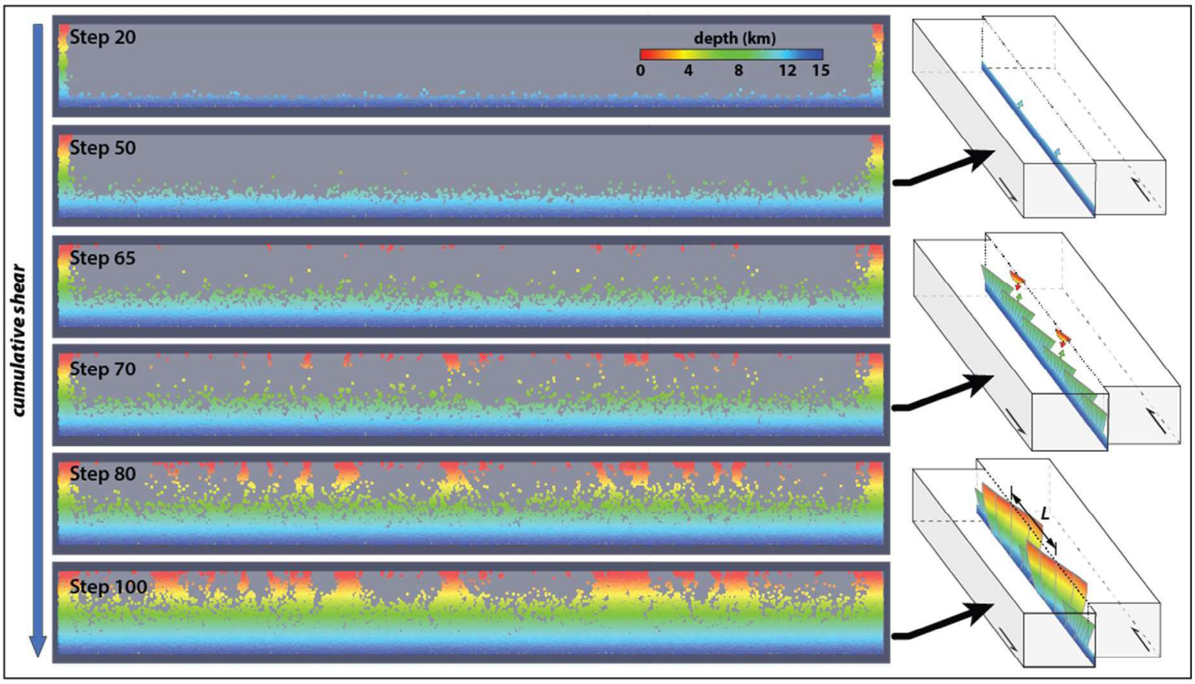

Figure 3: Successive 2km-wide swath cross-sections along the shear direction for increasing shear deformation at the base of the DEM model. Each dot indicates an induced crack colored according to its depth. Step 65 shows nucleation of crack clusters near the layer surface, which later expand downward to form Riedel shears. Sketches to the right illustrate time evolution of cracking within the brittle layer: 1) initiating from the base and propagating upward, 2) propagation both from top and base of crack fronts, and 3) formation of Riedel shears. L indicates the segment length.

4 State of stress on a plane between two Riedel-shear fractures

Under strike-slip loading conditions, and due to shear induced dilation, the horizontal stress state at the base of the plane ABA'B' located in-between 2 Riedel-shears (Fig. 4a) is primarily of tensile nature (Fig. S7). Building on previous experiments designed to study joint distribution in layered brittle materials (Taixu Bai and Pollard, 2000; T Bai *et al.*, 2000; Yang *et al.*, 2020; Zuza *et al.*, 2017), we set up a 2D elastic model to further investigate the state of stress on the plane ABA'B', as a function of the ratio R between the segment length (AA'), and the layer thickness (AB). The simplified 2D model consists of a layer with a free surface at the top, subjected to pure extensional loading at its base, in order to mimic the deformation process at play in between Riedel-shears (Fig. 4a). Because vertical deformations along AB and A'B' are fixed equal to zero, the extensional loading at the base induces some bending along the vertical axis that in turn generates compression in the ABA'B' plane in the vicinity of the vertical boundaries.

Figures 4b to 4d show the horizontal stress distribution along the vertical strike plane for different values of R=AA'/AB. By convention, compressional stresses are positive. When R≤1.5, the stress close to the surface is compressional (Fig. 4b and additional examples in Fig. S9). When R≥1.5, however, the stress at the surface becomes tensional (Fig. 4c and 4d, and Fig. S9). The tensile strength of brittle rocks is significantly lower than their compressive strength, and does not exceed few tens of MPa for crustal rocks (Cai, 2010). Thus, when tensional stress dominates at the surface of the layer, its tensile strength is almost immediately overcome and tension cracks nucleate. These cracks then propagate downward (Fig. 3; also animation A1) to link up with the cracks originating in the vicinity of the basal shear zone, and to form a new Riedel-shear. The creation of this newly-generated Riedel-shear reduces the value of R to a value lower than ~1.5 which, in turn, brings back the stress in a compressional state. The threshold value for R might vary depending on the tensile strength of the materials at play but, nevertheless, this variation stays within a 10% range for rocks (Cai, 2010). A similar process has been found responsible for crack saturation in layered sedimentary rocks and has been characterized by Bai and Pollard (2000). Fig. 4e shows the variation of the horizontal stress at the point M (Table S3), located in the middle of the layer surface, as a function of the ratio R. When the thickness is significantly larger than the length (ratio R equal to 0.3 or smaller), the stress at point M is close to zero. For R between ~0.3 and ~1.5, compressional stress dominates at point M. As soon as R becomes larger than ~1.5, tensional stresses dominate at point M and the system is unstable, leading to the appearance of a new Riedel-shear and to the subsequent decrease of R to a value close to 1.5. Thus, R~1.5 corresponds to a stable configuration where no additional Riedel would form. Therefore, the thickness of the brittle layer, by controlling the state of stress along the shear plane, exerts direct control over the segment length.

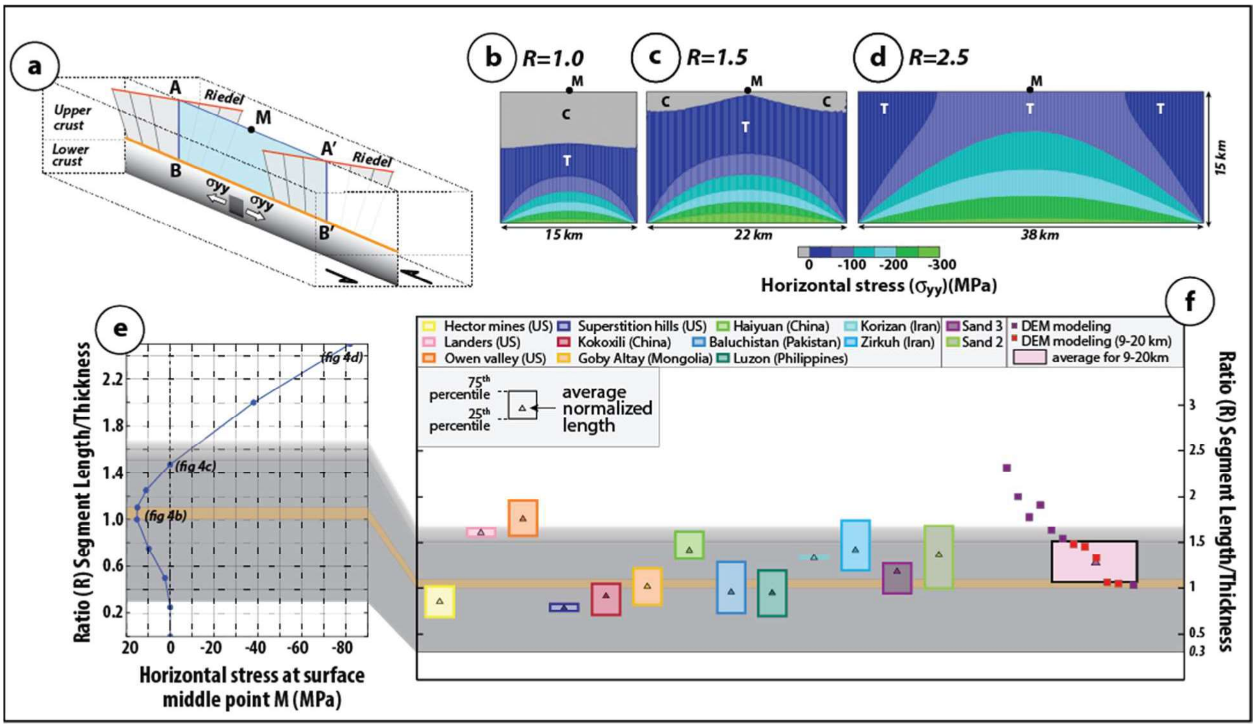

Figure 4: a) Conceptual model where strike-slip imposed at the base induces extension on the plane AA'BB' between two Riedel shears. b) to d) Horizontal stress ditribution (T for tension and C for compression) on the plane AA'BB' as a function of R=L/T, with L the segment length AA' and T the thickness AB=A'B'. Scenario d) is presented only to illustrate stress distribution for R>>1.5, since this configuration is unrealistic as material would already have ruptured. e) Horizontal stress at the surface middle point M as a function of R. The shaded area indicates values of R for which M is in a compressional state of stress. The maximum compressive stress is observed for R~1. Surface tensile cracks are generated for R≥1.5 when the tensile strength of the brittle layer is overcome (between 0 an 10 MPa depending on material). f) Comparison of R values measured in earthquake observations (after Klinger 2010), sandbox experiments (after Lefevre et al., 2020), and the present study (the pink polygone indicates average for thickness values generally acceped for the continental crust). In each case data are included into the compressional domain.

5 Comparison between field observations, analogue modeling, and numerical results

Figure 4f shows a compilation of data derived from earthquake-rupture field measurements (Klinger, 2010), from analogue fault segmentation experiments (Lefevre *et al.*, 2020), and from our numerical experiments. The values of the ratio R between segment length and thickness of seismogenic crust for continental earthquakes range between 0.3 and 1.6, well within the range predicted by the 2D elastic model. The data derived from DEM models and analogue models are also within the range predicted by the 2D model. Some of the DEM model data, however, fall significantly above the maximum predicted value. This is indeed expected as in both experiments, while one tests a wide range of thickness, one also departs from the mechanical parameter self-consistency that is needed when building a model behaving like the Earth brittle crust. For the models that are in a reasonable range with real brittle crust thickness (9 km $\leq T \leq$ 20 km), however, we find that the data also fall into the same range of values for the ratio R (1.1 < R < 1.5). Figure 4f demonstrates that a universal physical process controls the length of fault segments between successive Riedel-shears in different materials subjected to shear, including the crust of the Earth. Fault segmentation in earthquake ruptures is thus directly correlated to the thickness of the crust.

Acknowledgments

Observational datasets for that research are included in (Klinger, 2010; Lefevre *et al.*, 2020).

We thank J. McBeck, an anonymous reviewer, and the editor G. Prieto for insightful comments that helped improve this manuscript. The research was partly supported by the ANR project DISRUPT (ANR-18-CE31-0012). L.J. was funded by SIGMA-2 project.

References

Bai, T., and D. D. Pollard (2000), Fracture spacing in layered rocks: a new explanation based on the stress transition, Journal of Structural Geology, 22(1), 43-57.

Bai, T., D. Pollard, and H. Gao (2000), Explanation for fracture spacing in layered materials, Nature, 403(6771), 753-756.

Bilham, R., and P. Williams (1985), Sawtooth segmentation and deformation processes on the southern San Andreas fault, California, Geophys. Res. Lett., 12, 557-560.

Bischoff, P. H., and S. Perry (1991), Compressive behaviour of concrete at high strain rates, Materials and structures, 24(6), 425-450.

Cai, M. (2010), Practical estimates of tensile strength and Hoek–Brown strength parameter m i of brittle rocks, Rock Mechanics and Rock Engineering, 43(2), 167-184.

Cambonie, T., Y. Klinger, and V. Lazarus (2019), Similarities between mode III crack growth patterns and strike-slip faults, Philosophical Transactions of the Royal Society A, 377, doi: 10.1098/rsta.2017.0392.

Conner, R., W. L. Johnson, N. Paton, and W. Nix (2003), Shear bands and cracking of metallic glass plates in bending, Journal of applied physics, 94(2), 904-911.

Cundall, P. A., and O. D. L. Strack (1979), A discrete numerical model for granular assemblies, Geotechnique, 29(1), 47 - 65.

Duriez, J., L. Scholtès, and F.-V. Donzé (2016), Micromechanics of wing crack propagation for different flaw properties, Engineering Fracture Mechanics, 153, 378-398.

Fournier, T., and J. Morgan (2012), Insights to slip behavior on rough faults using discrete element modeling, Geophysical research letters, 39(12).

Francfort, F., and J. J. Marigo (1998), Revisiting brittle fracture as an energy minimization problem, J. Mech. Phys. Solids, 46(8), 893 -896.

Hart, R., P. A. Cundall, and J. Lemos (1988), Formulation of a three-dimensional distinct element model—Part II. Mechanical calculations for motion and interaction of a system composed of many polyhedral blocks, paper presented at International Journal of Rock Mechanics and Mining Sciences & Geomechanics Abstracts, Elsevier.

Hentz, S., F. V. Donzé, and L. Daudeville (2004), Discrete element modelling of concrete submitted to dynamic loading at high strain rates, Computers & structures, 82(29-30), 2509-2524.

Klinger, Y. (2010), Relation between continental strike-slip earthquake segmentation and thickness of the crust, J. Geophys. Res., 115, doi: doi:10.1029/2009JB006550.

Lefevre, M., P. Souloumiac, N. Cubas, and Y. Klinger (2020), Experimental evidence for crustal control over seismic fault segmentation, Geology.

Liu, Y., and H. Konietzky (2018), Particle‐Based Modeling of Transtensional Pull‐Apart Basins, Tectonics, 37(12), 4700-4713.

Lynch, J. C., and M. A. Richards (2001), Finite element models of stress orientations in well‐developed strike‐slip fault zones: Implications for the distribution of lower crustal strain, Journal of Geophysical Research: Solid Earth, 106(B11), 26707-26729.

Maggi, A., J. A. Jackson, D. McKenzie, and K. Priestley (2000), Earthquake focal depths, effective elastic thickness, and the strength of the continental lithosphere, Geology, 28(6), 495 - 498.

Mandl, G. (1999), Faulting in brittle rocks: an introduction to the mechanics of tectonic faults, Springer Science & Business Media.

Morgan, J. K. (1999), Numerical simulations of granular shear zones using the distinct element method: 2. Effects of particle size distribution and interparticle friction on mechanical behavior, Journal of Geophysical Research: Solid Earth, 104(B2), 2721-2732.

Morgan, J. K., and M. S. Boettcher (1999), Numerical simulations of granular shear zones using the distinct element method: 1. Shear zone kinematics and the micromechanics of localization, Journal of Geophysical Research: Solid Earth, 104(B2), 2703-2719.

Naylor, M., G. t. Mandl, and C. Supesteijn (1986), Fault geometries in basement-induced wrench faulting under different initial stress states, Journal of structural geology, 8(7), 737-752.

Potyondy, D. O., and P. Cundall (2004), A bonded-particle model for rock, International journal of rock mechanics and mining sciences, 41(8), 1329-1364.

Scholtès, L., and F.-V. Donzé (2013), A DEM model for soft and hard rocks: role of grain interlocking on strength, Journal of the Mechanics and Physics of Solids, 61(2), 352-369.

Scholz, C. (1990), The Mechanics of Earthquakes and Faulting, 439 pp., Cambridge University Press, New York.

Segall, P., and D. Pollard (1980), Mechanics of discontinuous faults, Journal of Geophysical Research: Solid Earth, 85(B8), 4337-4350.

Šmilauer, V., E. Catalano, B. Chareyre, S. Dorofeenko, J. Duriez, N. Dyck, J. Elias, B. Er, A. Eulitz, and A. Gladky (2015), Yade documentation 2nd ed. the yade project, edited, DOI.

Taheri, M., J. A. Barros, and H. Salehian (2020), Integrated approach for the prediction of crack width and spacing in flexural FRC members with hybrid reinforcement, Engineering Structures, 209, 110208.

Thomas, R. J., and A. D. Sorensen (2017), Review of strain rate effects for UHPC in tension, Construction and Building Materials, 153, 846-856.

Wechsler, N., Y. Ben-Zion, and S. Christofferson (2010), Evolving geometrical heterogeneities of fault trace data, Geoph. J. Int., 182, 551 - 567., doi: doi: 10.1111/j.1365-246X.2010.04645.x.

Wei, S., et al. (2011), Surficial simplicity of the 2010 El Mayor-Cucapah earthquake of Baja California in Mexico, Nature Geoscience, 4, 615-618, doi: 10.1038/NGEO1213.

Yang, H., L. N. Moresi, and M. Quigley (2020), Fault spacing in continental strike-slip shear zones, Earth and Planetary Science Letters, 530, 115906.

Zuza, A. V., A. Yin, J. Lin, and M. Sun (2017), Spacing and strength of active continental strike-slip faults, Earth and Planetary Science Letters, 457, 49-62.

Supplementary Materials for

Fault segmentation pattern controlled by thickness of brittle material

Liqing Jiao[1]; Yann Klinger[1*]; Luc Scholtès[2]

*Correspondence to: klinger@ipgp.fr

This PDF file includes:

Supplementary Note 1: DEM methodology

Figures S1-S9

Table S1-S3

Animations A1 caption

References (1-9)

Supplementary Note 2: Additional information on boundary effect in 3D models and 2D model assumptions

Other Supplementary Materials for this manuscript includes the following:

Animations A1

Supplementary Note 1: DEM methodology

1. Formulation

Following the principles of the DEM, the constitutive material of the crust is treated as a polydisperse assembly of interacting spherical discrete elements, also called particles (Figure S1a). The behavior of this synthetic crust material is thus governed by the motion of its particles and by the way they interact one with another. Here, following the approach proposed by *Scholtès and Donzé* (Scholtès and Donzé, 2013), we enable near neighbor interactions between non-strictly contacting particles so that interparticle bonds are created between pairs of particles when the following condition is fulfilled:

$$D_{AB}^{0} \leq \gamma(R_A + R_B)\,,$$

with R_A and R_B the radii of the interacting particles, D_{AB}^{0} the initial distance between their centroids, and $\gamma \geq 1$ the interaction range coefficient. The radii of particles are following the normal distribution (Figure S1b). This feature was used here for its capability to reproduce rheological characteristics of competent (brittle) rock-like materials (see (Scholtès and Donzé, 2013) for details).

The rheology of the simulated medium is governed by the force-displacement laws defined at the interparticle scale (Figure S1c and S1d). The interparticle forces are decomposed into a normal and a tangential component.

The normal contact law accounts for both divergence and convergence regimes (Figure S1e).

In the convergence regime (compression of the bond), the normal force F_n is computed as:

$$F_n = k_n \cdot U_n\,,$$

with $U_n = (D_{AB} - D_{AB}^{0})$ the normal component of the relative displacement between particles A and B, and k_n the normal stiffness derived from the properties assigned to the particles, such that:

$$k_n = \frac{2 \cdot Y_A \cdot R_A \cdot Y_B \cdot R_B}{Y_A \cdot R_A + Y_B \cdot R_B}\,,$$

with Y_A and Y_B the respective elastic moduli of the interacting particles.

In the divergence regime (extension of the bond), the normal force is computed with the same stiffness as the one used in the convergence regime but, unlike into the convergence regime, the interparticle force cannot increase infinitely. Instead, a maximum admissible tensile force F_n^{max}, associated to a yielding distance $U_n^{tensile}$, is defined:

$$F_n^{max} = t \cdot A_{int}\,,$$

with t the tensile strength of the interparticle bond and $A_{int} = \pi \cdot (min(R_A, R_B))^2$ the interacting surface area between A and B. When F_n^{max} is reached, the force is not set to zero immediately. Instead, F_n decreases gradually following a softening behavior when $U_n^{tensile} < U_n < U_n^{rupture}$, such as:

$$F_n = F_n^{max} - \frac{k_n}{S}(U_n - U_n^{tensile}),$$

with S a weakening coefficient. When $U_n > U_n^{rupture}$, the interparticle bond breaks and all forces are set to zero. A crack is then defined at the location of the bond breakage.

As in classic DEM formulations (Hart *et al.*, 1988), the tangential force F_s (Figure S1f) at the current time step *t* is computed incrementally such as:

$$F_s^{(t)} = F_s^{(t-\Delta t)} + k_s \cdot \Delta U_s \,,$$

with $F_s^{(t-\Delta t)}$ the force computed at the previous time step,ΔU_s ΔU_s the incremental tangential displacement between A and B, and k_s the tangential stiffness, defined as $k_s = P \cdot k_n$$K_s = a \cdot K_n$. As for the normal force, a maximum admissible tangential force F_s^{max} is defined as:

$$F_s^{max} = c \cdot A_{int} \,,$$

with *c* the interparticle cohesion. In our model, interparticle bonds do not break in shear. Instead, the tangential force stays equal to its maximum value until the maximum admissible normal force is reached.

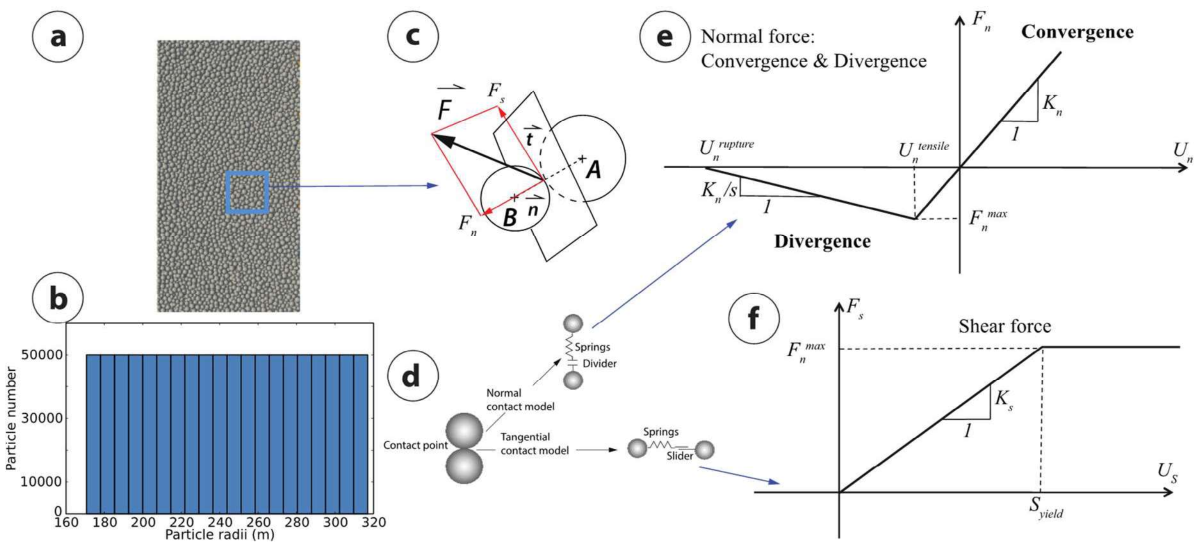

Supplementary Figure S1. The DEM model: (a) the material is treated as an assembly of bonded particles, (b) particle size distribution shows the radius of particle following a normal distribution range from 170 to 310 m, (c) illustration of the contact geometry shows normal and shear contacts between bonded particles, (d) interparticle force displacement models shows the normal and shear cases, (e) and (f) shows the calculation of the normal and shear force-displacement laws: K_n, K_s are the normal and shear stiffnesses between particles, U_n, U_s are the normal and shear distance between particles, F_n, F_s are the normal and shear forces between particles, $U_n^{tensile}$ is the yield normal distance, $U_n^{rupture}$

is the limited normal distance, S_{yield} is the yield shear distance, F_n^{max} and F_s^{max} are the maximum admissible tensile and tangential forces.

The calculation cycle of the DEM can be decomposed into four main steps related to, respectively, the determination of the particles' positions, the characterization of their potential interaction, the computation of the forces applying on them, either body forces or contact forces, and the calculation of their updated positions through the integration of the equations of motion (Newton's second law). This calculation cycle is repeated iteratively until the simulation ends. In addition, a non-viscous local damping is used to dissipate kinetic energy and to facilitate convergence of the system towards quasi-static equilibrium. The damping directly applies to the forces $\vec{F}$ that acts on the particles, so that acceleration of particles is calculated from the damped force

$$\sum \vec{F}^{(t)} - \alpha\, sign\left(\sum \vec{F}^{(t)}.\left(\vec{v}^{(t)} + \frac{dt}{2}\vec{a}^{(t)}\right)\right)\sum \vec{F}^{(t)},$$

where $0 < \alpha < 1$ is the damping coefficient, $\vec{v}^{(t)}$and $\vec{a}^{(t)}$the particle velocity and acceleration respectively, and dt the time step. This damping is a convenient numerical tool to ensure the convergence of the simulations that needs to be used with caution. As shown by (Duriez *et al.*, 2016), the damping coefficient value can have a quantitative influence on the strength of the simulated material. As usually done in DEM modeling, we kept α constant ($\alpha = 0.4$ here) throughout the entire study to prevent any quantitative bias in our analyses.

2. Geometry

Our objective was to simulate strike slip faulting in the continental crust considering depths T varying from 3 km to 30 km. In order to ensure a reasonable description of the deformation processes at stake in such a medium, we packed total 1 million discrete elements in our numerical sandbox of dimensions 160x40x32 km (Fig. S2), resulting in a resolution $6 < \frac{T}{D} < 60$ depending on the thickness considered (*D* means the mean diameter of particles which is equal to ~500 m, and particle radii are homogeneously distributed between 170 m and 320 m as shown in Figure S1b).

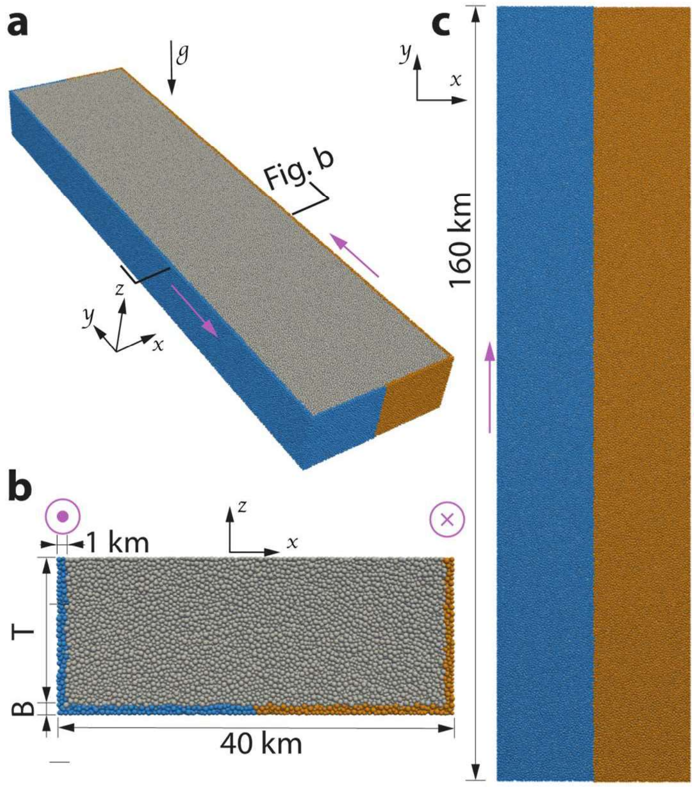

Supplementary Figure S2: Discrete element model setup: (a) 3D view, (b) Cross-section and (c) bottom view. The grey body represent the synthetic crust encased in between two rigid half boxes (blue and yellow) that move relatively to each other, along a localized strait boundary at the bottom of the model. The yellow boundary moves left-laterally related to the blue boundary (moving directions shown with purple arrows). *T* is the model thickness. B is the bottom boundary thickness. B is adjusted to model different crustal thickness with the same initial set-up by incorporating more particles into the bottom to change the thickness of the model without having to recompute a starting model from scratch for each crustal thickness. Hence, for different crustal thicknesses, the statistical distribution of particle sizes does not change, although the actual number of particles available is different.

3. Calibration

In order to simulate the behavior of the continental crust in this approach, the model needs to be calibrated. The calibration procedure of DEM models consists in adjusting the set of interparticle parameters so that the emergent macroscopic behavior is representative of the targeted medium behavior. The behavior of the seismogenic crust is typically brittle elastic with a pressure dependent strength (Scholz, 1990). To determine the relevant set of interparticle parameters for simulating the brittle crust behavior, we ran a series of triaxial compression tests simulations on a sample of the crust assembly under different confining pressures. We considered confining pressures varying from 0 to 800

MPa in order to be representative of the depth of the seismogenic crust (up to 30 km according to the interpretation given by (Klinger, 2010; Maggi *et al.*, 2000). Following the calibration procedure proposed by (Scholtès and Donzé, 2013), we finally settled on the set of interparticle parameters presented in Table S1 which produces the macroscopic mechanical behavior presented in both Table S1 and Figure S3.

We made the choice here to calibrate the emergent behavior of our synthetic crust to the behavior of a typical igneous rock (*e.g.*, a granite) with a Young modulus of ~10 MPa and a uniaxial compressive strength of ~150 MPa. As expected for cohesive-frictional materials, the compressive strength of our analog material is pressure dependent: it increases up to 2 GPa when the confining pressure is equal to 800 MPa.

Although simulating the continental crust as a strong brittle and competent rock is a classic procedure in rock mechanics, it is an assumption that should not be overlooked since it is likely that scale effects exist in nature and that such a large volume of material might not demonstrate identical mechanical properties than a sub-meter scale rock sample.

***Supplementary Table S1*: DEM model parameters and emergent bulk properties**

DEM model parameters	
Particle radius R	245±75 m
Particle density* ρ^p	4219 kg/m^3
Interaction range coefficient γ	1.5
Elastic modulus Y	45 GPa
Stiffness coefficient P	0.1
Tensile strength t	45 MPa
Cohesion c	45 MPa
Weakening coefficient s	5

* $\rho^p = \rho \frac{1}{(1-n^{pack})}$ with n^{pack}=0.36, the porosity of the assembly

Emergent bulk properties (simulated crust)	
Density ρ	2700 kg/m^3
Young's modulus E	10 GPa
Poisson's ratio ν	0.16
Uniaxial compressive strength UCS	150 MPa

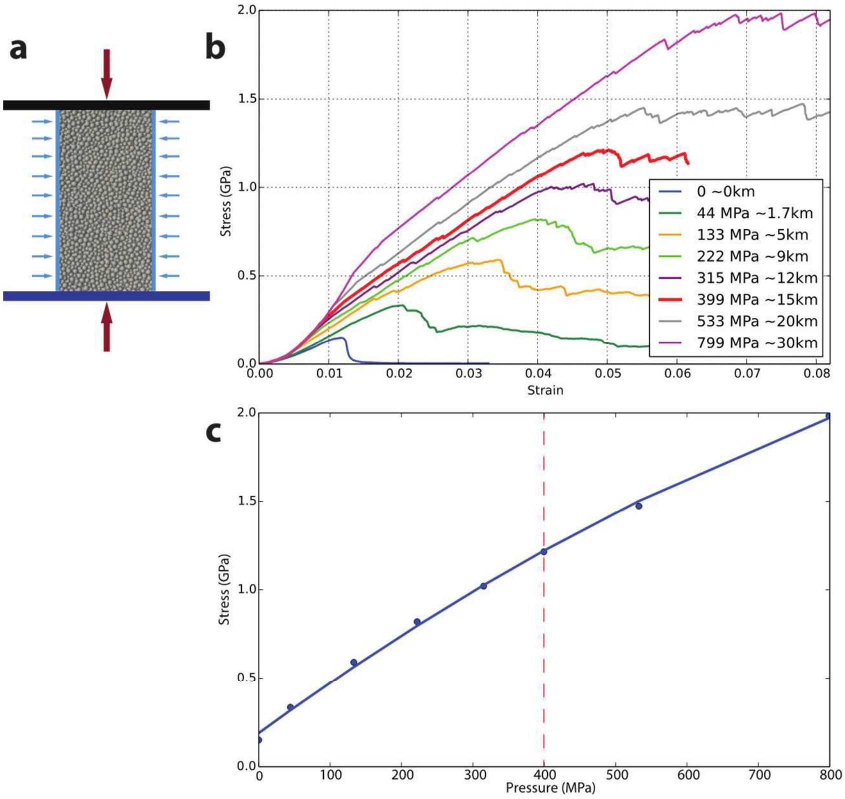

Supplementary Figure S3: Triaxial compression test simulations performed on the calibrated model (see Table S1): a) setup. b) stress-strain responses obtained for different confining pressures corresponding to different depths up to ~ 30 km (800 MPa). c) Relationship between the compressive strength of the simulated crust and the confining pressure (failure envelope). The red dashed line indicates the brittle-ductile transition which corresponds to a confining pressure of 400 MPa (depth of ~ 15 km).

4 Loading rate

To ensure the quasi-static behavior (Fig. S4) of the model's response, we imposed a strike-slip velocity of 0.25 m/s in all our simulations. The model being 160 km long, the corresponding strain rate is equal to 1.56×10^{-6} s^{-1}. According to the literature, such a strain rate ensures a quasi-static deformation for brittle materials(Bischoff and Perry, 1991), and is consistent with what is applied in numerical modeling (Hentz *et al.*, 2004; Thomas and Sorensen, 2017).

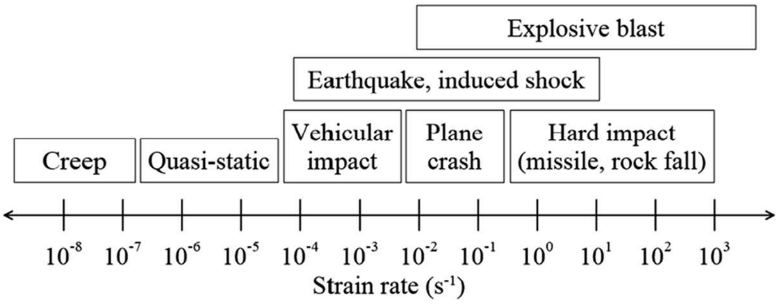

Supplementary Figure S4: Typical strain rate ranges for brittle materials (Hentz *et al.*, 2004)

In addition, we verified the rate independency of the model's behavior, by performing the same simulation with a higher loading rate equal to 2.5 m/s. As shown in Figure S5, the simulated fault patterns obtained for both loading rates are similar, confirming therefore that the model's response is quasi-static.

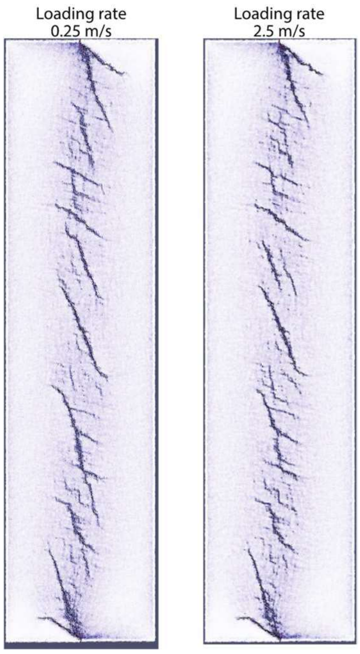

Supplementary Figure S5: Numerical results obtained for the same crust model with two different loading rates respectively equal to 0.25 m/s (left) and 2.5 m/s (right). The difference in deformation pattern is not significant.

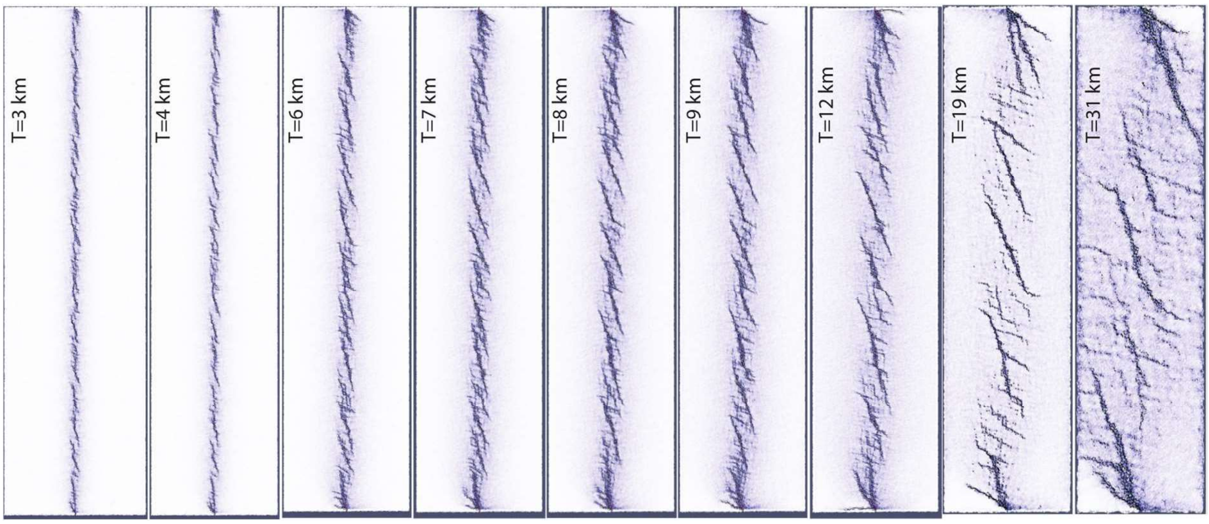

Supplementary Figure S6*: Fault pattern as a function of thickness *T

En-echelon fault patterns at the surface of models with different thicknesses *T* just before the en-echelon faults connect. The corresponding strike-slip displacements of the different models with *T*=3 km, 4 km,

Thickness (km)	No. of segments(mean)	No. of segments (low)	No. of segments (high)	segment length(mean) (km)	Segment length (low) (km)	segment length (high) (km)	Ratio(mean)	Ratio(low)	Ratio(high)
31	5	4	6	32	26.667	40	1.032	0.860	1.290
19	8	7	9	20	17.778	22.857	1.053	0.936	1.203
15	10	9	11	16	14.545	17.778	1.067	0.970	1.185
12	10	9	11	16	14.545	17.778	1.333	1.212	1.481
10	11	10	12	14.545	13.333	16	1.455	1.333	1.6
9	12	11	13	13.333	12.308	14.545	1.481	1.368	1.616
8	13	12	14	12.307	11.429	13.333	1.538	1.429	1.667
7	14	13	15	11.428	10.667	12.308	1.633	1.524	1.758
6	14	13	15	11.428	10.667	12.308	1.905	1.778	2.051
5	18	17	19	8.889	8.421	9.412	1.778	1.684	1.882
4	20	19	21	8	7.619	8.421	2	1.905	2.105
3	23	22	24	6.957	6.667	7.273	2.319	2.222	2.424

6 km, 7 km, 8 km, 9 km, 12 km, 19 km and 31 km are respectively equal to 42.4 m, 51 m, 94.8 m, 121.2 m, 138.8 m, 156.4 m, 174 m, 174 m and 182.8 m. In these numerical experiments, only the thickness *T* of the model was varied, all other parameters were kept constant. Models with thicknesses T<3 km could not produce observable en-echelon faults due to the model's resolution.

Supplementary Table S2.

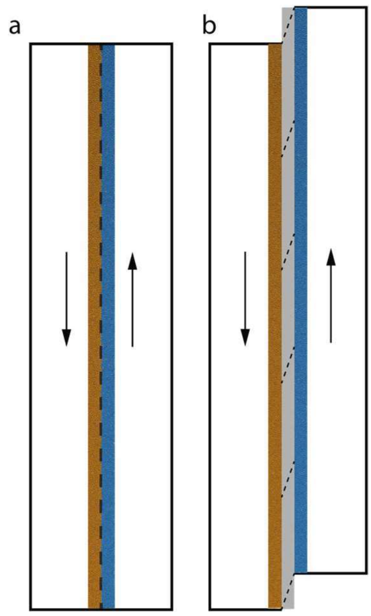

Supplementary Figure S7: Schematic cartoon showing the tension zone that develops along the strike-slip fault: a) before strike-slip motion; b) during strike-slip motion. The vertical plane located above the strike-slip fault is in a tensional state.

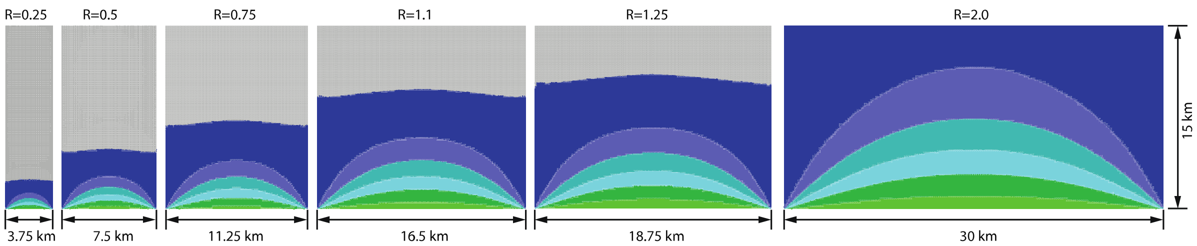

Supplementary Figure S8: Distribution of the horizontal stress (σ_{yy}) along the strike direction for different ratios (R=L/T) of the inter segment spacing length *L* to the layer thickness *T*. See Fig. 4b to 4d for caption.

Supplementary Table S3

Ratio of the spacing length to the thickness	Horizontal stress at the centre of the surface (Point M) (MPa)
0	0
0.25	0.008
0.5	2.4
0.75	9.8
1	15.2
1.1	15
1.25	11
1.47	0.02
2	-38
2.5	-82
3	-131

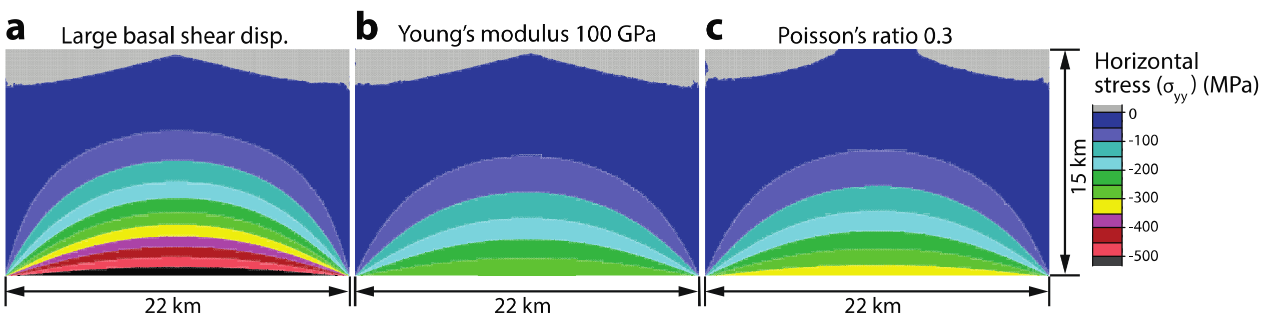

Supplementary Figure S9: Example of sensitivity of horizontal stress output for input parameters different from the parameters used in our main work (shown in Fig. 4c and also listed in table S1): a) Basal shear displacement twice as large as in our working model b) Young's modulus five times larger than the value set in the working model, and c) Poisson's ratio twice as large as in the working model. Any other model setup and boundary conditions are kept the same as in the working model.

Animations S1: Model evolution for increasing shear deformation. Micro-cracks appear when the tensile strength of the material is overcome. The micro-cracks are color-coded according to their depth, similarly to figure 3.

References

Bischoff, P. H., and S. Perry (1991), Compressive behaviour of concrete at high strain rates, Materials and structures, 24(6), 425-450.
Duriez, J., L. Scholtès, and F.-V. Donzé (2016), Micromechanics of wing crack propagation for different flaw properties, Engineering Fracture Mechanics, 153, 378-398.
Hart, R., P. A. Cundall, and J. Lemos (1988), Formulation of a three-dimensional distinct element model—Part II. Mechanical calculations for motion and interaction of a system composed of many polyhedral blocks, paper presented at International Journal of Rock Mechanics and Mining Sciences & Geomechanics Abstracts, Elsevier.
Hentz, S., F. V. Donzé, and L. Daudeville (2004), Discrete element modelling of concrete submitted to dynamic loading at high strain rates, Computers & structures, 82(29-30), 2509-2524.
Klinger, Y. (2010), Relation between continental strike-slip earthquake segmentation and thickness of the crust, J. Geophys. Res., 115, doi: doi:10.1029/2009JB006550.
Maggi, A., J. A. Jackson, D. McKenzie, and K. Priestley (2000), Earthquake focal depths, effective elastic thickness, and the strength of the continental lithosphere, Geology, 28(6), 495 - 498.
Scholtès, L., and F.-V. Donzé (2013), A DEM model for soft and hard rocks: role of grain interlocking on strength, Journal of the Mechanics and Physics of Solids, 61(2), 352-369.
Scholz, C. (1990), The Mechanics of Earthquakes and Faulting, 439 pp., Cambridge University Press, New York.
Thomas, R. J., and A. D. Sorensen (2017), Review of strain rate effects for UHPC in tension, Construction and Building Materials, 153, 846-856.

Supplementary Note 2: Why Finite Difference Model (FDM) technics cannot be used to address the issue of the state of stress along the fault plane between two successive Riedels.

Although this part is not directly needed to go through our work, following the reviewers we though that it might be interesting for a reader more specifically interested in the modeling details to see what guided our methodological choice.

1: Why 3D FDM model cannot be used to explore the stress field between two successive Riedels?

For question 1, the short answer is impossible to make 3D FDM model to address this issue, since the model could not avoid the boundary effect.

In this work, our purpose is to observe the state of the maximum principal stress in plane along the main strike-slip fault, in between two successive Riedel shears.

We try to set up a 3D FDM model (Figure S2.1a). In our model settings, we prevent any vertical displacement along the bottom of the model, only allowing for horizontal displacement along the y-axis of one half of the model.

The main issue is to decide on the boundary conditions at both ends of the model, where the strike-slip fault intersects with the Riedel-shears (here set at 90° from strike-slip for sake of simplicity. One example with a smaller angle is also presented at the end that illustrates that this parameter is not relevant here): Here we have tested two ways to set up the Riedel-shear boundary conditions: A/ free boundaries along the Riedel-shear, and B/ no vertical displacement allowed along the Riedel-shear

A/ 3D models with free boundaries along Riedel shears

First, we set up a 3D FDM model with free boundaries along the Riedel shears at both ends of the model (Figure S2.1a). One side of the model is moved at the velocity of 8.10^{-4} km/step, while the other side is fixed. After 2000 steps, the model shows that the maximum principal stress field along the fault zone is strongly affected by the stress distribution along the boundaries (Riedel shear) (Figure S2.1b, c, and d). If the distance between Riedel shear faults is smaller (such as the case in Figure S2.1b compared to the cases in c, and d), the boundary effect is even stronger. Conversely, when distance between the successive Riedel shear is increased, the boundary effect is fading away. However, such dependency by construction forbid to use this approach to study the state of stress on the fault plane in function of the distance between Riedel as the amount of contamination by boundary effects also depends on such distance.

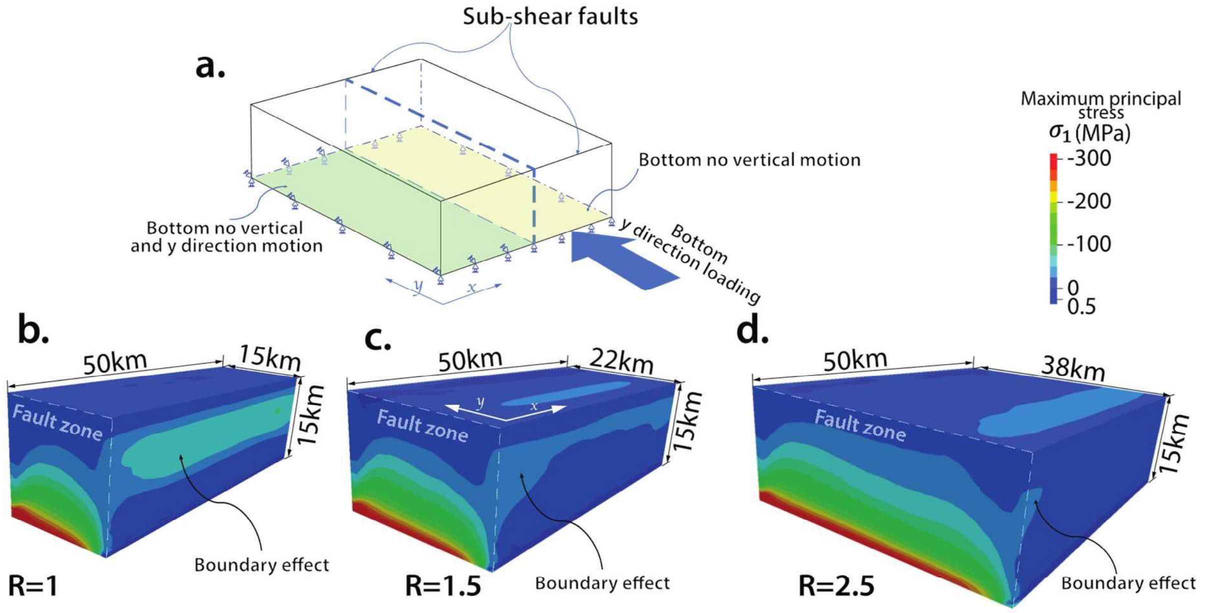

Figure S2.1. 3D FDM model settings with free boundaries along the Riedel shears and horizontally fixed one half of the bottom and moving another half of the bottom (**a**) and the maximum principle stress of the models with different distance between the Riedel shears (15, 22, and 38 km for **b**, **c**, and **d** respectively).

B/ 3D models with no vertical motion allowed along the Riedel shears

If we set up a 3D FDM model with no vertical direction (z direction) allowed along the Riedel shear faults (Figure S2.2a), the boundary effect is different, although still very strong (Figure S2.2b, c, and d), preventing to use this approach to solve our specific problem

For sake of completeness we set up one 3D FDM model where we have changed the angle between sub-shear fault and the main strike-slip fault to a smaller angle, 15°, closer to what is actually observed in nature or analogue models. Thus, we set a 15° Riedel shear fault from the strike of the strike-slip fault (Figure S2.2e). The model result (Figure S2.2f) shows that the boundary effect is still strong and that the angle between the strike-slip fault and the Riedel shear is not a critical parameter in that respect.

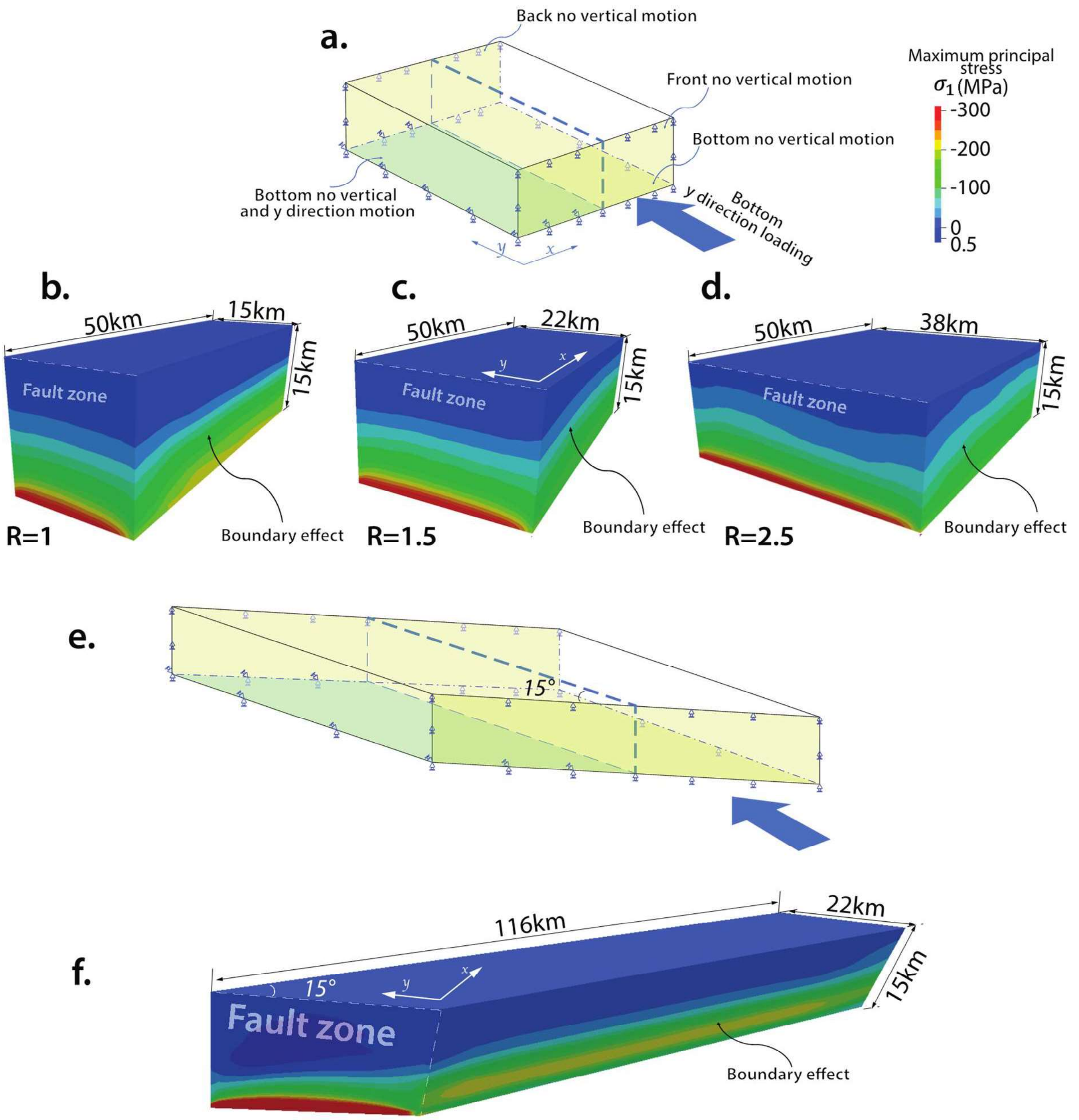

Figure S2.2. 3D FDM model settings with no vertical displacement allowed along the Riedel shears (**a**). **(b)** to **(d)**: The maximum principle stress of the models with different distance between pre-existing sub-shears (15, 22, and 38 km for **b**, **c**, and **d** respectively). 3D FDM model settings with 15° Riedel shears (**e**) and the maximum principal stress distribution of the model with a distance between successive Riedel shears of 22km (**f**).

Thus, these 3D FDM models show that wit this approach we could not avoid boundary effects in our simulations, meaning that this technique is not suitable for our purpose.

2: How to solve boundary effect issues to make a suitable model for the analysis of the stress field between Riedels?

To adress the main point of the study we had to built a 2D model, which focuses on the 2D fault plane corresponding to the main strike-slip fault in-between two Riedel shears (Figure 4a). The boundary conditions in this configuration are derived from our observations in both 3D FDM and DEM models: 1) no vertical displacement on the surface of the main strike-slip fault plane; 2) exert pure tension loading along the fault plane direction (s_{yy}) at the bottom; 3) no vertical displacement along the Riedels shear. Justification for such boundary condition in our 2D model are given below:

Surface boundary and loading settings based on 3D FDM model

The following 3D FDM model shows why it is a reasonable assumption to consider that there is no vertical motion along the strike-slip fault plane and why we could only consider tension at the surface:

The model settings are same as those in Figure S2.2a, with horizontal shear displacement at the base of the model along the y direction. From the 3D DEM model results, the vertical displacement field (Figure S2.3b) shows that vertical displacement is symmetrical relative to the fault plane and, in fact, it implies that vertical motion has to go through zero along the fault plane. Thus, in the simplified 2D model the vertical displacement is constrained to be zero on the fault plane (AA'BB'), as shown in Figure 4a of the paper.

Figure S2.3c shows the stress field along the y-axis of the fault for this model. We can see that the stress field is quite uniform in tension along that direction and, thus it is the reason why we set the tension stress at the bottom for the simplified 2D model in Figure 4a.

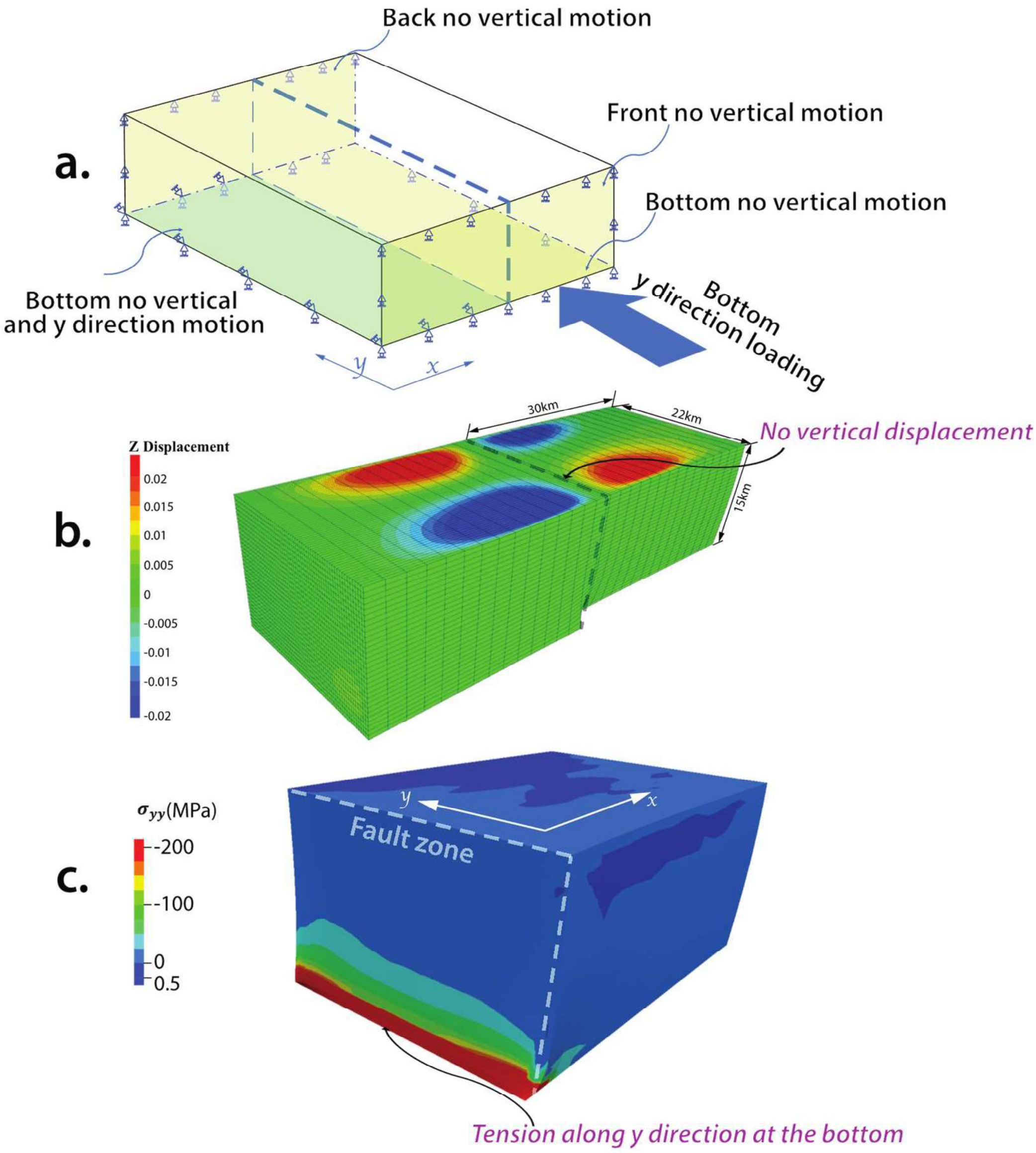

Figure S2.3. Horizontal displacement constrained to be along the Y-direction (**a**), which is same to Figure S2.2a. The vertical displacement on the surface shows the zero vertical displacement along the line above the main strike-slip fault located at the bottom (**b**). The horizontal stress field along the y direction shows the stretch along the y direction at the bottom (**c**).

Riedel shear boundary settings based on the 3D DEM models

Here we show why we need to prevent any vertical displacement along Riedels based on 3D DEM simulation. Figure S2.4 shows the vertical displacement field of a 3D DEM model. In order to show displacement change through deformation more clearly, we take an example, which has a larger distance between Riedels than in the models presented in the paper. Figure S2.4 shows the top view of the 3D DEM models. The distribution of the vertical displacement shows the zero displacement along the Riedels shear faults (Figure S2.4a) when the Riedels shears just initiate. Figure S2.4b is just for the comparison with Figure S2.4a, once the Riedel have developed. Figure S2.4c shows the vertical difference between the two time steps, emphasizing the effect of Riedels formation and the symmetrical deformation pattern across the Riedel, implying that vertical deformation has to go through zero when crossing the Riedel. This is in fact consistent with the observation from Figure S2.3b.

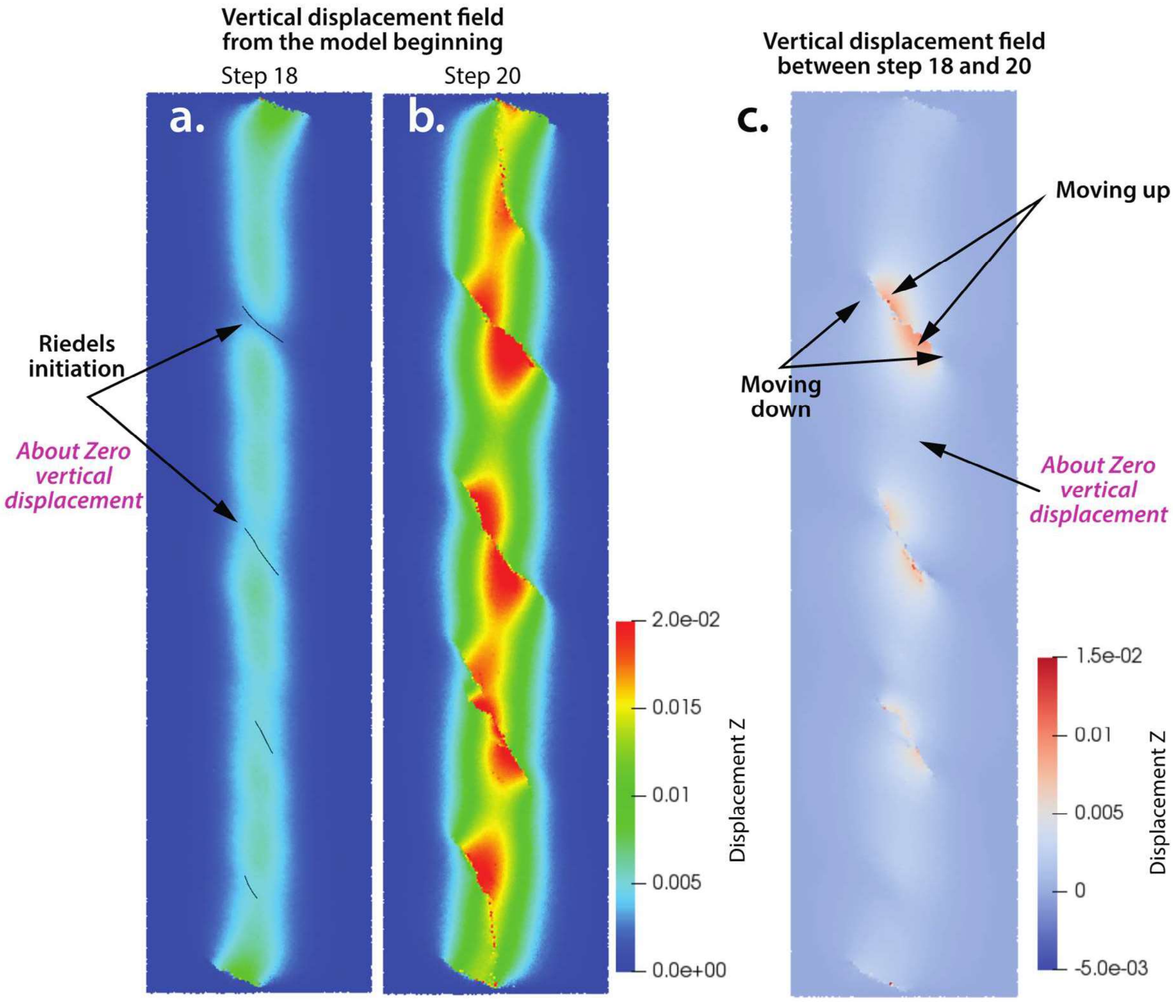

Figure S2.4. DEM model shows the vertical displacement field from the model beginning (just before the Riedels shears reach the surface at step 18 (**a**) and after they developed at step 25 (**b**)). These displacement fields show that the vertical displacement along the sub-shear fault (Riedels) at the surface is about 0 when the sub-shear faults just initiate on the surface. (**c**) shows the vertical displacement change before and after the sub-shear faults come to the surface. Along the Riedels, the one side of the tip is going up, while opposite side is going down, and vice-versa at the other end of the Riedel. Thus, the vertical displacement along the fault zone for a Riedel shear has to be zero.